Electrotextile-Based Flexible Electromagnetic Skin for Wearables and Remote Monitoring

Rossella Rizzo, Giuseppe Ruello, Rita Massa, Maxim Zhadobov, Giulia Sacco

IEEE Journal of Microwaves

Received 24 May 2024; revised 10 July 2024 and 18 September 2024; accepted 19 November 2024.

Digital Object Identifier 10.1109/JMW.2024.3504846

Electrotextile-Based Flexible Electromagnetic Skin for Wearables and Remote Monitoring

ROSSELLA RIZZO [1,2], GIUSEPPE RUELLO [2] (Senior Member, IEEE), RITA MASSA [3], MAXIM ZHADOBOV [1] (Senior Member, IEEE), AND GIULIA SACCO [1] (Member, IEEE)

(Regular Paper)

[1]Univ Rennes, CNRS, CentraleSupelec, Nantes Université, IETR UMR 6164, F 35000 Rennes, France
[2]Department of Electrical Engineering and Information Technology (DIETI), University of Naples Federico II, 80138 Napoli, Italy
[3]Department of Physics E. Pancini, University of Naples Federico II, 80138 Napoli, Italy

CORRESPONDING AUTHOR: Rossella Rizzo (e-mail: rossella.rizzo@univ-rennes.fr).

The funding formulation required by the European Union is: This work was supported in part by the European Union's Horizon Europe research and innovation program under Grant N°101063966 (Marie Skłodowska-Curie IN-SIGHT project); in part by the France2030 EUR DIGISPORT program under Grant ANR-18-EURE-0022 (WEARSPORT project); in part by the European Union through EU Regional Development Fund (ERDF); in part by the Ministry of Higher Education and Research, CNRS, Brittany Region, Conseils Départementaux d'Ille-et-Vilaine and Côtes d'Armor, Rennes Métropole, and Lannion Trégor Communauté, through the CPER Project CyMoCod; and in part by the French National Research Program for Environmental and Occupational Health of Anses under Grant 23-RF-07 CHILD-5G poject and Grant 23-RF-03 EXPO-5G project.

ABSTRACT This paper presents a flexible electrotextile-based solid skin-equivalent phantom operating in the millimeter-wave (mmW) range. The phantom reproduces the reflection coefficient at the air/skin interface in the 55–65 GHz band. It is composed of a layer of carbon powder mixed with silicone and backed with an electrotextile. Its thickness is optimized to approach the target reflection coefficient of the human skin. For the angles of incidence from 0° to 60° the maximum relative error in respect to the target value is 2.6% for the magnitude and 13% for the phase when considering impinging transverse electric (TE) and transverse magnetic (TM) polarized plane wave. To experimentally validate the phantom, its scattering properties are measured in the 55–65 GHz range using a free-space transmission/reflection system. A good agreement between the numerical and experimental results is demonstrated, exhibiting a relative error within 1.9% for the magnitude of the reflection coefficient in the 55–65 GHz range at normal incidence. Such phantoms may be used in a wide range of body-centric mmW applications, including remote sensing and medical applications.

INDEX TERMS Millimeter-wave (mmW), solid flexible phantom, electrotextile.

I. INTRODUCTION

Wireless sensors have emerged as an add-on to conventional wired network systems, in particular in medical applications [1]. These devices may be positioned on or in the vicinity of the body, for instance for remote monitoring of physiological activities. The unlicensed mmW band around 60 GHz [2] is promising for such applications due to low interference, high data rates and ultra-miniature dimensions.

To characterize the electromagnetic (EM) performance of body-centric radiating structures, they need to be tested in a controlled and reproducible way in real-case scenarios, ideally accounting even for posture as well as macro and/or microscopic body movements (resulting from heartbeat, breathing, etc.). For instance, this enables the on-body performance assessment of wearable sensors during physical activity or of radar sensors remotely measuring the motion of the chest associated with cardiorespiratory activity. Experimental tissue-equivalent phantoms play a crucial role in research and compliance testing due to the capability of reproducing the EM properties of biological tissues. Various phantom types have been proposed and categorized as liquid, semi-solid, and solid. Some examples are listed in Table 1, comparing the phantom type, the frequency range it's intended for and the measured properties.

TABLE 1. Skin-Equivalent Phantoms in the 0–100 GHz Range

Reference	Phantom type	Frequency range	Targeted physical quantity	Maximum standard deviation
[5]	Liquid	3.1–10.6 GHz	Relative path gain	1.4 dB
[6]	Liquid	2.4–2.48 GHz	ε_r	0.5%
			σ	3.4%
[7]	Liquid	0–3 GHz	ε_r	5%
			σ	5%
[22]	Liquid	0.5–18 GHz	ε_r	2%
			Loss factor	1.4%
[23]	Liquid	0.5–12 GHz	ε_r	0.7%
			σ	7.1%
[8]	Semisolid	55–65 GHz	ε_r	10%
			SAR at 60 GHz	1.3%
[24]	Semisolid	2–26.5 GHz	ε_r	5.6%
[25]	Semisolid	0.5–50 GHz	ε_r	22%
[26]	Semisolid	10–100 GHz	ε_r	16%
[27]	Solid	50 GHz	APD	15.7%

Liquid or gel phantoms typically consist of a container filled with a liquid or gel that replicates the EM properties of the human body or specific body parts [3], [4], [5]. The composition of a liquid phantom can vary depending on the emulated body part and on the frequency. At lower frequencies, such as those below 1 GHz, a mixture of sugar, deionized water, sodium chloride, and cellulose is typically used, while at higher frequencies (above 1 GHz and extending into the mmW range), mixtures of deionized water and a polyhydric alcohol or diacetin are common. Liquid phantoms can replicate the target dielectric properties of tissues with high accuracy over a wide frequency range. For example, in [6], the standard deviation is below 0.5% for the mixture's permittivity and below 3.4% for its conductivity when compared to the skin's values in the 2.4–2.48 GHz range. Liquid phantoms are particularly suitable for volumetric measurements using immersed probes. Application examples include in-phantom characterization of implantable wireless devices, assessing the specific absorption rate (SAR) and compatibility of in-body wireless devices. For instance, a liquid phantom simulating head and body tissues up to 3 GHz was reported in [7], exhibiting a maximum standard deviation of 5% in both its permittivity and conductivity, compared to the targeted values. This phantom was employed for dosimetry and densitometry measurements. A mixture of Triton X-100 and diethylene glycol butyl ether (DGBE) was used in [6] to replicate the dielectric properties of skin within the 2.4–2.48 GHz industrial, scientific, and medical (ISM) band and conduct in vitro measurements of an implantable antenna. The antenna was tested using the skin-mimicking material. In the 2.4–2.5 GHz frequency range, a liquid phantom was employed to validate the performances of a wearable antenna in a reverberation chamber [3].

Semisolid phantoms occupy a middle ground between liquid and solid phantoms in terms of viscosity and rigidity. One of their significant advantages is the possibility to manipulate their mechanical properties to reproduce the physical characteristics of tissues. Typical ingredients of semisolid phantoms include water, oil, gelatin powder, agar, and sodium azide. In contrast to the liquid ones, these phantoms can mimic more complex geometries (without a container), recreating anatomical shapes [8]. They also enable the creation of multi-layer structures [9]. As a result, semisolid phantoms are commonly employed for wearable technology and body area network (BAN) testing, dosimetry, and microwave imaging [8], [10], [11]. Agar-based phantoms have been effectively employed at radiofrequencies and mmW. For instance, an agar-based skin phantom was developed for BAN applications, emulating skin characteristics within the 55–65 GHz frequency range [8].

Solid phantoms possess several unique advantages compared to liquid and semisolid phantoms. This includes the possibility of creating complex shapes with high accuracy and an extended lifetime. However, replicating tissue properties necessitates specialized materials and often specific equipment for crafting solid phantoms [12], [13]. To shape solid phantoms, which often need to mimic anatomical structures, two main approaches are employed: they are either cured using a mold or initially cured in a basic form (e.g., a rectangular prism) and subsequently shaped into the desired anatomical geometry through machining. The ceramic-based phantoms, designed for assessing the SAR at 900 MHz through thermography, demonstrate the ability to closely match permittivity and loss tangent of the body across the majority of the phantom [14]. The conductive plastic phantoms are used for microwave near-field biological imaging arrays and are employed for validating microwave imagers [12]. Silicone rubber phantoms combined with various forms of carbon offer the ability to match the electrical properties of both high and low-permittivity tissues up to 6 GHz [15], [16]. These phantoms find applications in various fields, such as breast phantoms for microwave imaging and on-body testing of 4G/5G antennas. A solid phantom made of a silicone substrate containing carbon black powder was proposed in [17] to characterize the on-body propagation channel at 60 GHz. This phantom has been specifically designed to match the reflection coefficient at the air/phantom interface to that of the air/skin interface.

Due to their water-free nature, solid phantoms are not subject to evaporation or hardening of the surface, so their properties are stable over time. In [18] bonding resin composites loaded with powder additives are used to emulate the dielectric properties of head tissues in the 0.5–5 GHz range. Its lifetime stability was investigated, comparing it to a gelatin/water phantom. The results showed no changes in the dielectric properties of the resin-based phantom, and a decrease of 45% in the dielectric properties of the water-based phantom three days after fabrication.

During the years, 3D-printed tissue-equivalent phantoms have emerged as an alternative to molding in medical imaging, dosimetry, and biomedical research. These phantoms are designed to mimic the EM properties of human tissues, providing a versatile and cost-effective solution. The fabrication of these phantoms involves the use of common 3D printing methods, which allow for rapid prototyping and customization of objects from a variety of materials. For instance, studies have demonstrated the feasibility of creating breast and soft tissue-equivalent phantoms using thermoplastic materials like polylactic acid (PLA) and acrylonitrile butadiene styrene (ABS) by carefully adjusting printing parameters such as infill density and pattern [19], [20]. For example, in [21] PLA filaments with different concentrations of nanoparticles are 3D printed with the fused deposition modeling (FDM) technique to represent a multi-layer model of the skin. This phantom was used to assess the thermal effects of electromedical radiofrequency (RF) fields on human tissues.

In this paper, we propose the first electrotextile-based skin-equivalent solid mmW phantom for performance testing of on-body wireless devices, characterization of body-centric propagation channel and performance validation, under well-controlled and reproducible conditions, of radar systems designed for remote sensing of physiological activities. It is flexible, which makes it particularly well adapted for reproducing curved body parts. In addition, the phantom thickness is within a few millimeters, enabling reproducing micro-movements of the body surface, emulating for example heart beating or breathing.

II. PHANTOM DESIGN

At mmW, given the high dielectric contrast between the skin and free space, a considerable fraction of the impinging power is reflected at the air/skin interface. For instance, at 60 GHz, the reflection coefficient hovers around 60% for the normal incidence [28]. This value varies depending on the polarization and angle of incidence [29] between 0.2 to 1 for TM mode and from 0.6 to 1 for TE mode. To experimentally emulate the scattering properties of the human skin, one possibility is to realize a phantom whose complex permittivity is close to that of the skin ($\varepsilon_r = 7.98 - j \cdot 10.9$) at 60 GHz [30]). However, given the high losses at these frequencies, it is challenging to reproduce these permittivity values with bulk solid phantoms. Some solid mmW phantoms are available on the market and serve various purposes, including SAR evaluation, optimizing on-body and implant transceivers, as well as validating

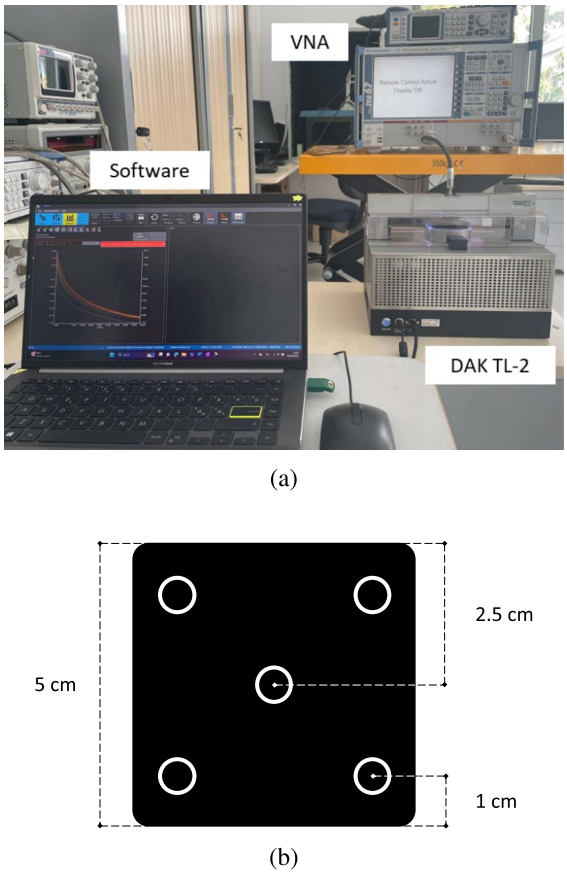

FIGURE 1. (a) Experimental setup used to measure the dielectric properties of the carbon-silicone composite. (b) Position of the on-phantom measurement points (white rings).

simulation models [31], [32]. These phantoms are usually quite stiff, making it difficult to adapt them to different shapes and limiting their ability to mimic the natural movements of the body surface. An alternative approach involves crafting a thin structure with a reflection coefficient matching that of the skin, paving the way to flexible and conformal phantoms. Achieving the desired properties in solid phantoms involves incorporating conductive and high-permittivity additives into a lower-permittivity base material (e.g., plastic or silicone) during curing. For this purpose, we designed a phantom composed of a silicone material (SYLIGARD 184) mixed with carbon black powder and backed with an electrotextile. The latter is a flexible fabric that acts as a ground plane ($\sigma = 1.96 \cdot 10^5 S/m$). It also acts as a shield, making the phantom robust and insensitive to the presence of an object that may be positioned behind the phantom.

A. COMPLEX PERMITTIVITY MEASUREMENT

The first step of the phantom design is the characterization of the dielectric properties of the silicone and carbon mixture in a wide range of frequencies that will be later used as an input for the phantom reflection coefficient optimization to estimate the target thickness. The measurement setup [Fig. 1(a)], primarily comprises a dielectric assessment kit (DAK) TL-2,

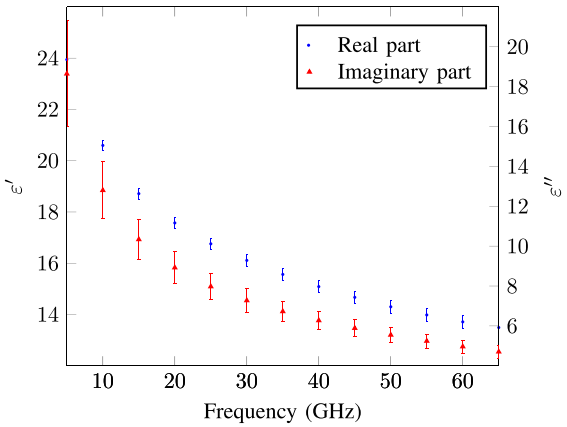

FIGURE 2. Real and imaginary part of the measured complex permittivity of a mixture of silicone and carbon (40%).

a vector network analyzer (VNA), and the control software. The DAK TL-2 is a coaxial probe-based system that enables the automatized characterization of the dielectric properties of solid and semi-solid materials, including thin sheets (0.1–10 mm), as well as liquid samples. This system utilizes open coaxial probes and, in addition to S_{11} measurements, performs automated measurements of thickness and mechanical force. The dielectric properties of the material under examination are derived from S_{11} measured at the probe flange, accounting for the sample thickness. The measurements are performed in the 5–65 GHz range. The system was calibrated using a copper strip used as a short and alumina-N5 as a reference load. A thickness calibration is performed using a 2 mm metal sample.

Measurements are performed for samples containing 40% of carbon. This weight ratio between carbon and silicone was chosen as a compromise between the necessity to increase the complex permittivity to reach the target reflectivity and the need to maintain its elastic properties. The sample is placed on the designated support and subjected during the measurement to 200 N force. 20 permittivity measurements are performed at different points of the sample's surface to verify its homogeneity and reproducibility [Fig. 1(b)]. Fig. 2 shows the mean value and the standard deviation of the permittivity's real and imaginary parts, as a function of frequency. The real part exhibits a maximum standard deviation of 1.8%, while for the imaginary it reaches 14.2%. At 60 GHz the standard deviation is 1.7% and 6.6% for the real and the imaginary part, respectively. The reference value is established as the average of the 20 measurements [$\varepsilon_r = 13.7 \cdot (1 - j \cdot 0.36)$ at 60 GHz].

The dielectric properties of the phantom have been measured again one year after the initial fabrication of the samples, the standard deviation between the two sets of measurements is below 1%.

B. ANALYTICAL MODEL OF THE PHANTOM

To expedite the investigation of the EM phantom properties, we developed an analytical transmission line model in MATLAB. Two interfaces are considered: air/silicone-carbon and silicone-carbon/electrotextile [Fig. 3(a)]. The last segment of the line is short-circuited to represent the electrotextile sheet and t is the thickness of the silicone-carbon layer. The impedances for free space and the silicone-carbon layer are calculated both for TM [Fig. 3(b)] and TE [Fig. 3(c)] modes as

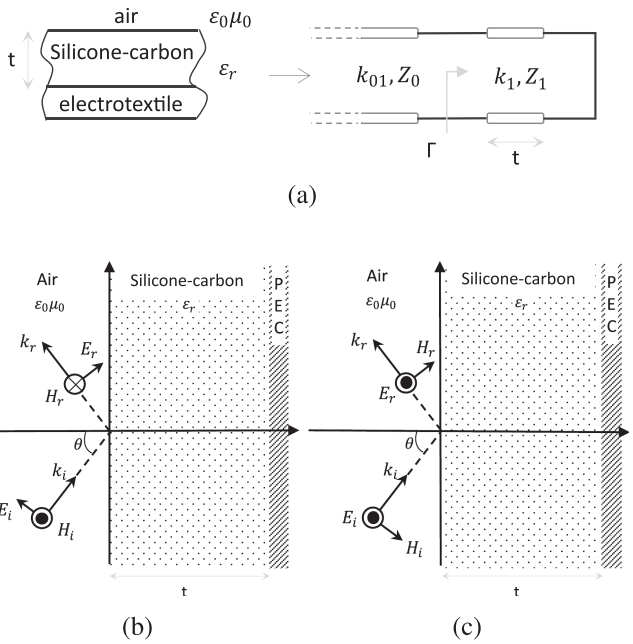

FIGURE 3. (a) Analogy of the phantom with a transmission line terminated in a short circuit. Modes: (b) TM and (c) TE.

$$Z_{0_{\mathrm{TM}}} = \frac{k_{01}}{\omega\varepsilon_0}, \qquad Z_{1_{\mathrm{TM}}} = \frac{k_1}{\omega\varepsilon_0\varepsilon_r}, \tag{1}$$

and

$$Z_{0_{\mathrm{TE}}} = \frac{\omega\mu_0}{k_{01}}, \qquad Z_{1_{\mathrm{TE}}} = \frac{\omega\mu_0}{k_1}. \tag{2}$$

Here $k_{01} = k_0 \cdot \cos\theta$ and $k_1 = k_0\sqrt{\varepsilon_r - \sin^2\theta}$, where θ is the incidence angle, $k_0 = \omega\sqrt{\varepsilon_0\mu_0}$ is the free space wave number, $\varepsilon_0 = 8.854 \cdot 10^{-12}$ F/m, $\mu_0 = 4\pi \cdot 10^{-7}$ H/m, ε_r is the complex permittivity of the silicone-carbon composite, and ω is the angular frequency.

The reflection coefficient is given by the following equation:

$$\Gamma = \frac{Z(t) - Z_0}{Z(t) + Z_0}, \tag{3}$$

where $Z(t) = j \cdot Z_1 \cdot \tan(k_1 \cdot t)$ is the transformed impedance at a distance t from the load and Z_0 and Z_1 are calculated using (1) or (2), depending on the polarization.

Varying the angle of incidence from 0° to 60°, the characteristic impedances are calculated for both TM and TE modes, using (1) and (2) respectively, and the corresponding reflection coefficient is computed with (3).

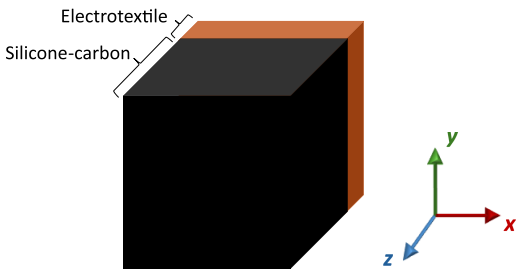

FIGURE 4. CST model of the phantom.

C. NUMERICAL MODEL OF THE PHANTOM

A numerical parametric study is performed using the finite element method (FEM) implemented in CST Microwave Studio. Supposing that the illuminated area of the phantom is sufficiently smaller than its total surface, the edge effects can be neglected and it can be modeled as an infinite surface. This is obtained by applying periodic boundary conditions in the x and y directions. We simulate an infinite surface by periodically extending the elementary unit cell. This approach can significantly reduce computational resources and simulation time compared to modeling the entire structure. The dimension of the unit cell in the x- and y- axis are 1 mm. In the z direction (perpendicular to the surface of the phantom), a perfectly matched layer (PML) is applied to simulate an open non-reflecting environment. The phantom model consists of two homogeneous layers: the first layer is composed of silicone-carbon and the second one consists of electrotextile (Fig. 4). The thickness of the silicone-carbon layer is varied from 1 mm to 8 mm and its complex permittivity is the one established in Section II-A. The electrotextile is a lossy metal with a conductivity of $\sigma = 1.96 \cdot 10^5 S/m$ and a thickness of 0.17 mm. The incident wave is modeled as a default plane wave with a frequency of 60 GHz, considering both TM and TE modes. The angle of incidence is varied from 0° to 60°, allowing for comprehensive analysis and comparison with the analytical model. A tetrahedral mesh is used, with a mesh size of approximately $\lambda/20$, where λ is the wavelength of the incident wave. This mesh setting provides a balance between accuracy and computational efficiency, and convergence tests confirmed the stability of the simulation results. The FEM is used to calculate the reflection coefficient at the air/phantom interface.

The transmission line equivalent model has been validated by comparing the analytical reflection coefficient to the one obtained through numerical simulations, for the incidence angles in the 0–60° range, showing excellent agreement.

D. ANALYTICAL MODEL OF THE SKIN

The transmission line equivalent model can also be used to calculate the reflection coefficient at the air/skin interface, considering the skin homogeneous structure.

Given a high water content of the epidermis and dermis, mmW energy experiences a rapid attenuation and more than 90% is absorbed before reaching the fat layer [33]. To confirm the possibility of using a homogeneous medium to represent the skin at 60 GHz, we compared a multilayer and a monolayer model. Table 2 summarizes the key dielectric properties of both models. Fig. 5 illustrates the comparison between the power reflection coefficient for TM and TE modes, calculated using both the multilayer model and the monolayer structure. An excellent agreement between the two models is observed, hence, for our application, the skin can be represented by a monolayer model, with the complex permittivity extracted from [30].

Fig. 6 shows the transmission line model of the skin, represented by a semi-infinite homogeneous structure. Its characteristic impedances, respectively for TM and TE modes are

$$Z_{\text{skin}_{\text{TM}}} = \frac{k_{\text{skin}}}{\omega \varepsilon_0 \varepsilon_{\text{skin}}}, \tag{4}$$

TABLE 2. Typical Properties of Multilayer and Monolayer Skin Models at 60 GHz

		ε'	σ (S/m)	Thickness (mm)
Multilayer	Stratum corneum	2.96	10^{-4}	0.015
	Epidermis + dermis	7.98	36.4	1.45
	Fat	3.13	2.8	1
Monolayer		7.98	36.4	-

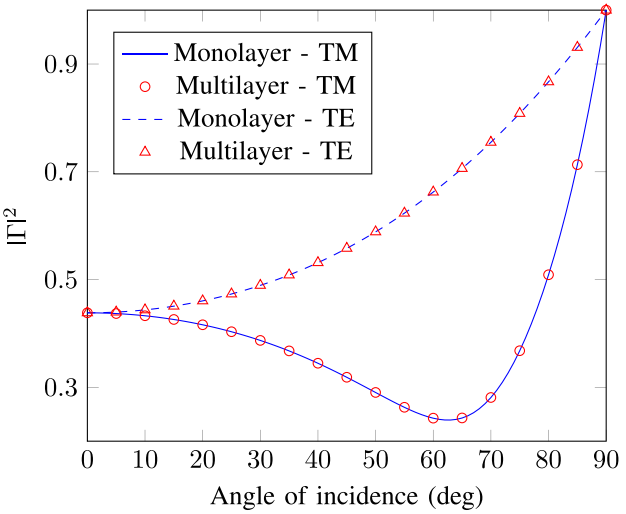

FIGURE 5. Power reflection coefficient of the monolayer and multilayer skin models.

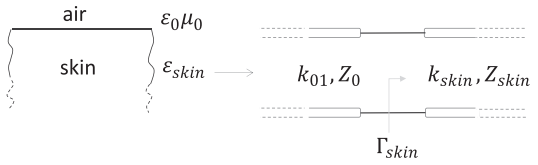

FIGURE 6. Analogy of the skin with a transmission line.

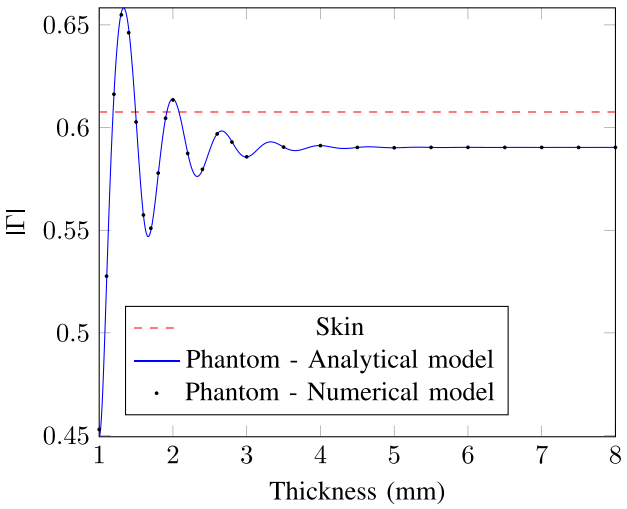

FIGURE 7. Magnitude of the reflection coefficient of the silicone-carbon phantom and skin for the normal incidence as a function of the phantom thickness.

and

$$Z_{\text{skin}_{\text{TE}}} = \frac{\omega\mu_0}{k_{\text{skin}}}, \tag{5}$$

where $k_{\text{skin}} = k_0\sqrt{\varepsilon_{\text{skin}} - \sin^2\theta}$ and $\varepsilon_{\text{skin}} = 7.98 - j{\cdot}10.9$. [30] The reflection coefficient at the air/skin interface is:

$$\Gamma = \frac{Z_{\text{skin}} - Z_0}{Z_{\text{skin}} + Z_0}, \tag{6}$$

E. OPTIMAL THICKNESS DEFINITION

Given the multiple reflections occurring at the air/silicone-carbon and silicone-carbon/electrotextile, the reflection coefficient exhibits a damped sinusoidal behavior. Fig. 7 represents the magnitude of the reflection coefficient as a function of the thickness of the silicone-carbon layer for the normal incidence. A stable value is reached around a thickness of 4 mm, meaning that the reflection coefficient does not depend anymore on the silicone-carbon layer thickness. The analytical data of the phantom and the skin reference are calculated using the transmission line equivalent model and considering the incidence angle $\theta = 0°$. The numerical data are obtained through simulations performed with a normally incident plane wave and they are in good agreement with the analytical ones. The choice of normal incidence is intended to demonstrate the behavior of the reflection coefficient, which exhibits a damped sinusoidal pattern due to the constructive and destructive interference from multiple internal reflections within the silicone-carbon layer. This behavior is consistent across all angles of incidence, although the positions of the minima and maxima shift with the angle. Note that at the normal incidence, the reflection coefficient does not depend on the polarization of the incident wave. This is because, at normal incidence, the electric and magnetic fields of the wave are oriented such that the boundary conditions are identical for TE and TM modes [34].

The analytical approach was employed to find the optimal phantom thickness. The transmission line models described in Section II-B and Section II-D, are used to calculate the reflection coefficient of the phantom and of the skin, respectively. Both TM and TE modes are taken into account. The optimization aims to minimize the deviation between the reflection coefficient at the air-phantom interface and the one at the air-skin interface. To this end, the analytically calculated magnitude and phase of the skin's reflection coefficient for incidence angles in the 0–60° range are used as the targeted values. The thickness of the silicone-carbon layer was varied from 1 mm to 3 mm, with 0.1 mm increments. For each specific thickness within this range, taking the skin as a reference, the relative error is computed as:

$$\text{relative error}_{\%} = \left|\frac{f(\theta)_{\text{phantom}} - f(\theta)_{\text{skin}}}{f(\theta)_{\text{skin}}}\right| \times 100 \tag{7}$$

where $f(\theta)$ is either the magnitude or the phase of the reflection coefficient computed across angles of incidence spanning from 0° to 60°, with a 5° step width. Fig. 8 reports the relative error distributions as a function of the phantom thickness. The central red line in each bar is the median, the lower and upper boundaries of the box encapsulate the 25th and 75th percentiles, and the dashed lines denote the maximum and minimum value. The red data points situated outside the box denote outlier error values, mainly associated with the incidence angle of 60°. The TM mode exhibits higher relative errors, with average values reaching 45% in magnitude [Fig. 8(a)] and 30% in phase [Fig. 8(b)]. In TE mode, the relative amplitude error [Fig. 8(c)] is under 10% for most of the considered thicknesses, while it is consistently below this value for the phase [Fig. 8(d)].

The results suggest three optimal values of the phantom thickness: 1.5 mm, 2.1 mm, and 2.7 mm. However, according to the magnitude of the reflection coefficient, the 1.5 mm configuration is not robust enough to thickness uncertainty, with relative errors that can increase from 0.6% to 8.4% for a 0.1 mm difference in thickness, value comparable with the typical fabrication tolerance (0.1 mm). This behavior is a consequence of the resonance phenomenon shown in Fig. 7, which is responsible for stronger variations of the reflection coefficient for thinner phantoms. The 2.6–2.8 mm range of thicknesses is also promising, especially in terms of the magnitude of the reflection coefficient. However, among the three optimal thicknesses, this phantom would exhibit the worst flexibility. The thicknesses spanning from 2 mm to 2.2 mm offer more robustness to thickness uncertainty compared to the 1.5 mm case and a higher flexibility than the 2.7 mm case. For these three thicknesses, considering the magnitude of the reflection coefficient, the median relative error is in the 0.3–3% range for TM mode and varies between 0.6% and 2.5% for TE. Consequently, variations in thickness within this specific range will produce minimal alterations in the amplitude of the reflection coefficient. Considering the phase, the median of the relative error varies in the range 5.4–7% in TM mode

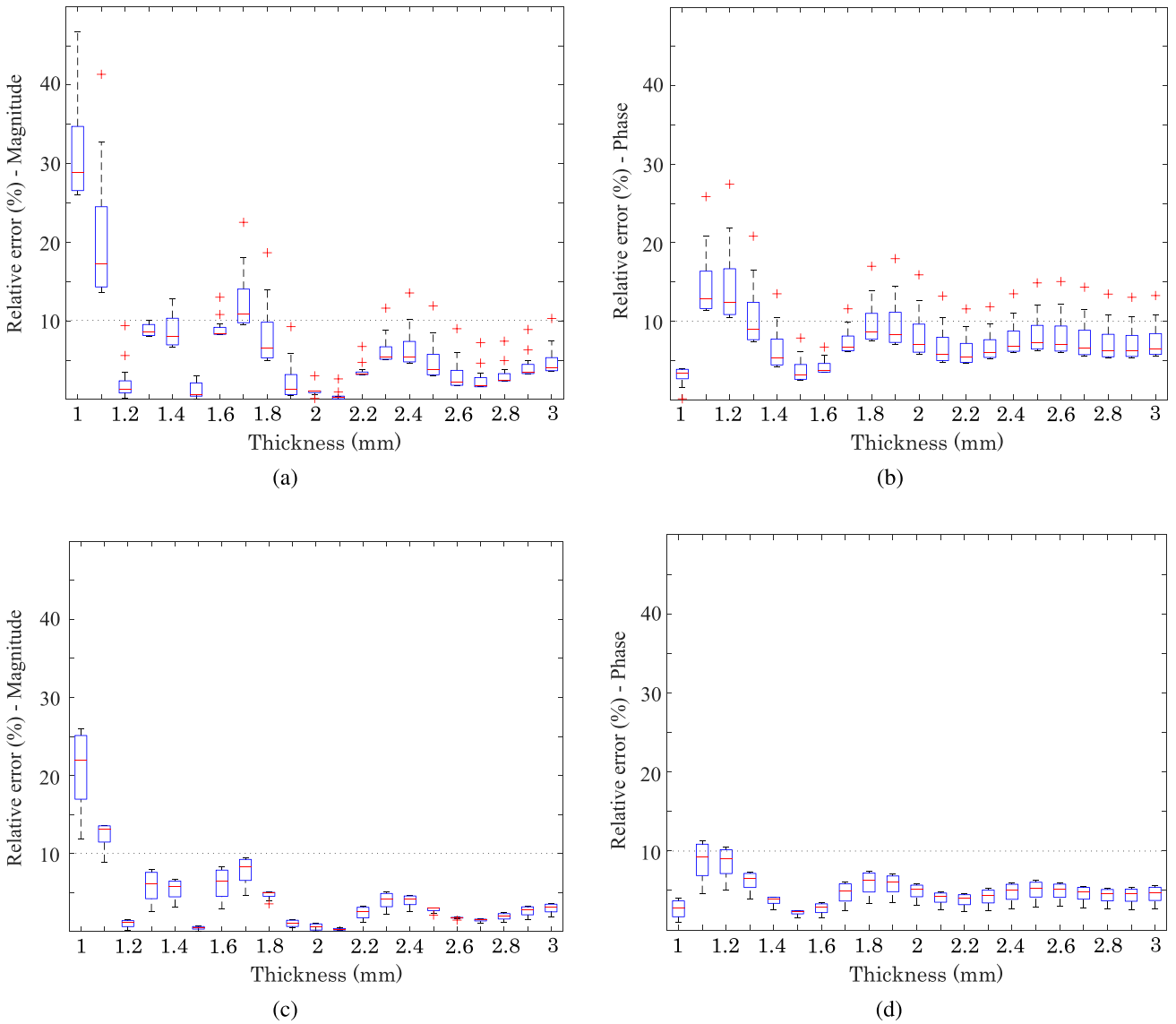

FIGURE 8. Distributions of the relative error of the phantom's reflection coefficient compared to that of skin. Top line - TM mode: (a) magnitude, (b) phase. Bottom line – TE mode: (c) magnitude, (d) phase.

and 4–5.2% in TE mode. The thickness of 2.1 mm is finally selected for the phantom design.

Comparing the reflection coefficient of the phantom to the one of the skin, for incidence angles in the range 0° to 60°, the maximum relative error for the amplitude [Fig. 9(a)] is 2.6% for TM and 0.4% for TE mode, while for the phase [Fig. 9(b)] it is 13% and 4.8% respectively. Note that these variations are within natural physiological variations, for instance as related to age or skin moisture [35], [36].

F. PERMITTIVITY UNCERTAINTY

To assess the impact of the uncertainty in the measured permittivity on the reflection coefficient at 60 GHz, a Monte Carlo analysis with 10^6 trials was conducted based on the dataset of 20 permittivity measurements, shown in Section II-A. We assumed that the real and imaginary parts of the permittivity follow a Student's t-distribution. With this hypothesis we computed the distributions of the magnitude and phase of the reflection coefficient for TE and TM modes for angles of incidence in the 0–60°range, every 5°. The resulting deviation from the mean value, with a 95% confidence level, consistently remained below 1% for the magnitude and phase of the reflection coefficient for both polarizations. This analysis underscores the reliability and robustness of the obtained results.

III. PHANTOM REALIZATION

To fabricate the phantom, the following materials are used:

- SYLGARD 184 Silicone Elastomer base [37];
- SYLGARD 184 Silicone Elastomer curing agent;
- Sigma-Aldrich 484164 Carbon powder [38];
- electrotextile.

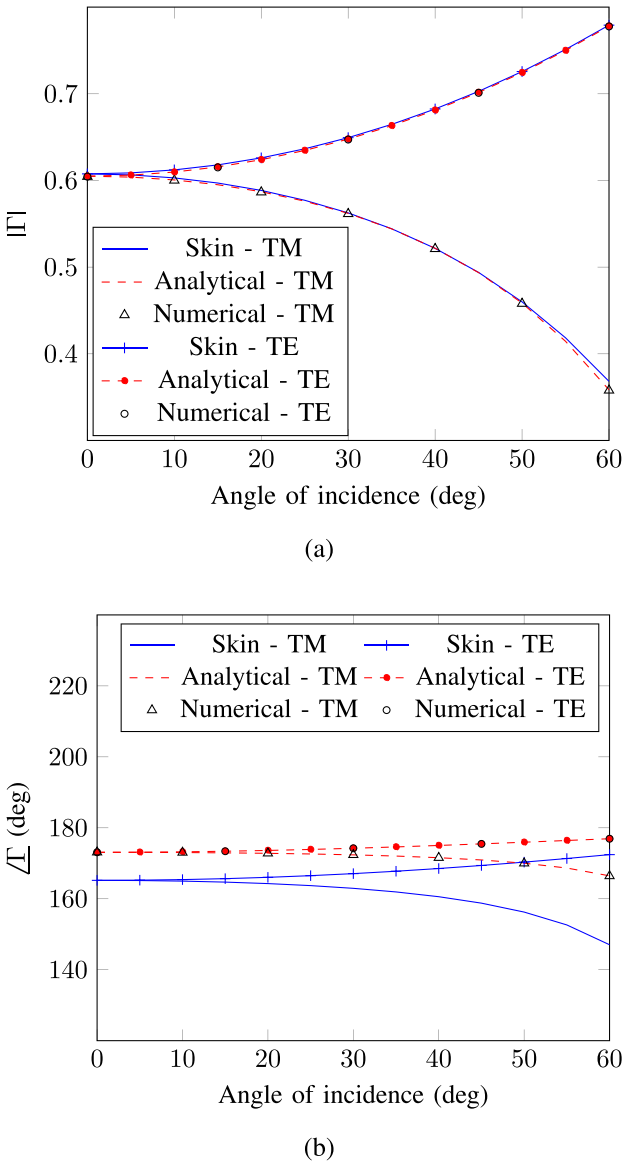

FIGURE 9. **(a) Magnitude and (b) phase of the reflection coefficient for skin and phantom models at 60 GHz for TM and TE modes.**

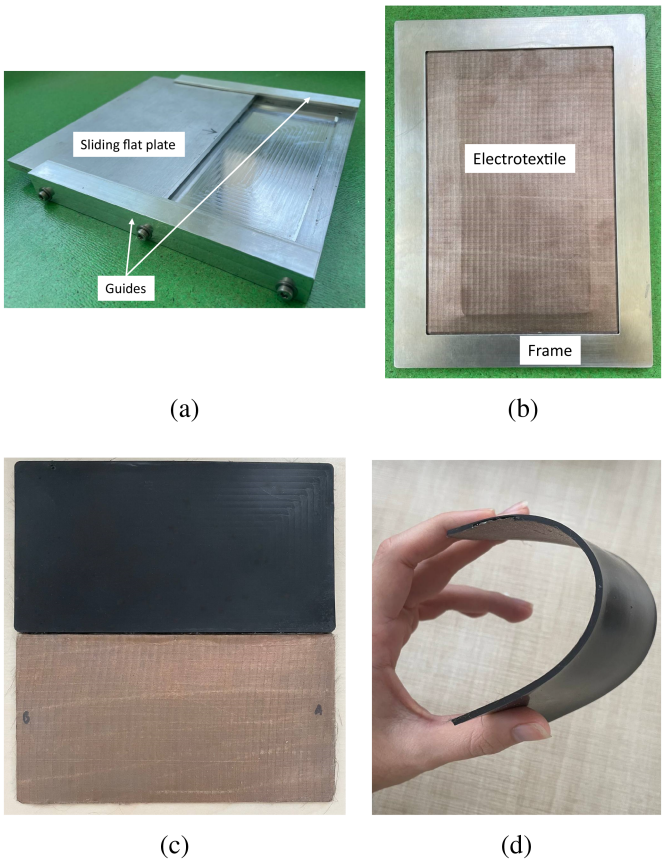

FIGURE 10. **(a) Mold and (b) frame used in the phantom fabrication process, (c) upper and bottom view of the fabricated phantom, (d) bent flexible phantom.**

The starting point is preparing the silicone by adding one part of the curing agent for ten parts of the base, followed by thorough mixing. Carbon is then added to the mixture progressively achieving 40% of the total weight of the composite. It is carefully mixed until it achieves homogeneity. The liquid composite is subsequently transferred into a mold [Fig. 10(a)] with a thickness of 2.1 mm. Then it is placed within a vacuum chamber for degassing (30 minutes) to remove air bubbles appeared during mixing. To improve the planarity of the phantom a flat plate is slid on the liquid composite to progressively seal the mold. Following the first degassing round, the chamber is opened, and the plate is slid over the surface of the phantom to cover a portion of the compound (approximately 2 cm). The silicone-carbon is then subjected to another round of degassing for 20 minutes. This cycle is repeated until the entire surface is covered by the plate. The mold is then transferred into an oven set at 110 °C for 2 hours, allowing the liquid composite to solidify. This procedure was tested using transparent silicone, which permits the detection of air bubbles. It was observed that some air may be retained in the first few millimeters of the composite sides, but the affected edge can be easily cut to eliminate bubbles from the phantom. Ultimately, this results in a phantom characterized by nearly constant thickness (relative variations within 5% in respect to the target thickness). To prevent folds, the silicone-carbon layer is placed on a flat surface and the textile is draped over it, ensuring it is stretched and secured with an interlocking frame [Fig. 10(b)]. Following this, pure silicone is prepared and poured onto the electrotextile. Pressure is applied to facilitate the passage of silicone through the textile and ensure proper adhesion to the silicone-carbon layer. The silicone is subsequently solidified in an oven set at 110 °C for an hour. Any exceeding silicone can be easily removed after it cools down.

The obtained fabricated phantom prototype is shown in Fig. 10(c) and (d). In summary, this fabrication method results in a flat phantom, ensuring controlled silicone-carbon layer thickness and minimizing the thickness of the silicone used to glue the electrotextile.

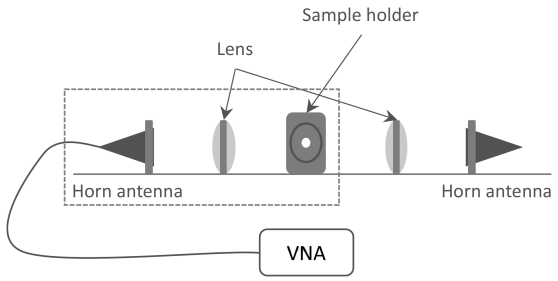

(a)

(b)

FIGURE 11. (a) Transmission/reflection quasi-optical setup (b) system used to measure the scattering parameters of the phantom.

IV. EXPERIMENTAL VALIDATION

As an experimental validation we measured the reflection coefficient of the fabricated phantom and compared it with the reflection coefficient of human skin. We used a free-space method employing a VNA and a transmission/reflection quasi-optical setup equipped with two focusing lenses and two horn antennas [Fig. 11(a)]. Since we need to measure the reflection coefficient, only one of the two ports of the system is used [part of the system delineated by the dashed rectangle in Fig. 11(a)]. The holder for the phantom has a hole with a radius of 1.5 cm, centered on the focal point of the lenses [Fig. 11(b)]. The calibration is performed with an empty sample holder and then with a metal plate.

The magnitude of the S_{11} is measured over a frequency range spanning from 55 GHz to 65 GHz and correlated with the magnitude of the reflection coefficient. Environmental interferences are eliminated by subtracting S_{11} associated with the metal plate. Phase measurements have not been performed with this system at this stage, due to the more critical positioning of the phantom required for accurate phase measurements. The magnitude of the reflection coefficient is then derived using the following formula:

$$|\Gamma_{\text{derived}}| = 10^{\left(\frac{S_{11\text{phantom}} - S_{11\text{plate}}}{20}\right)}. \quad (8)$$

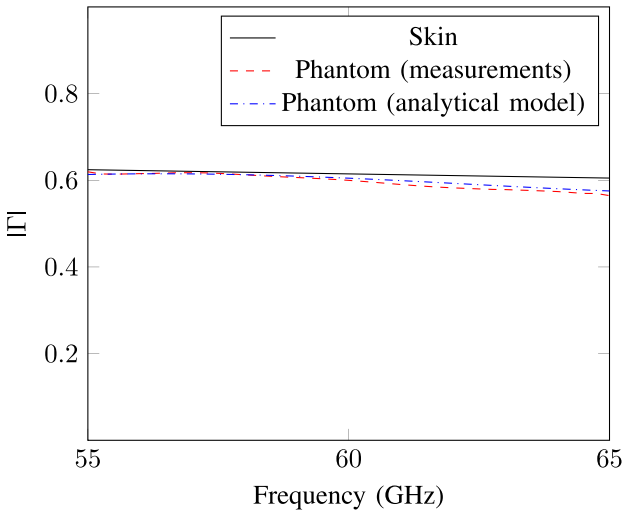

FIGURE 12. Magnitude of the reflection coefficient derived from the measurements compared to the coefficient of the skin and the coefficient calculated analytically in the 55–65 GHz range.

This coefficient is then compared to the reference reflection coefficient of human skin and the calculated one Fig. 12. The measured reflection coefficient is in good agreement with the one calculated employing the permittivity values acquired with the DAK TL-2 (relative deviation within 1.9%). In respect to the reflection coefficient of skin, the average relative error is below 3%, the maximum relative error is within 6.6%.

V. DISCUSSION AND CONCLUSION

In this work, we designed and experimentally validated the first flexible electrotextile-based phantom reproducing the scattering properties of human skin in the 55–65 GHz range. In contrast to the commonly used rigid bulk phantoms, flexibility is achieved by using electrotextile on a thin flexible dielectric substrate, which thickness is optimized to achieve scattering properties close to the ones of human skin (relative deviation within 2.6% for magnitude and 13% for phase at 60 GHz for 0–60°). The phantom demonstrates the enhanced robustness to the thickness uncertainty. The proposed fabrication procedure enables the fabrication of mechanically robust phantoms as the electrotextile is directly embedded into the silicon composite.

A proof-of-concept prototype was fabricated and its reflection coefficient was measured in the 55–65 GHz range (for normal incidence), showing relative error within 1.9% compared to the analytical phantom model and 6.6% compared to the skin's reflection coefficient.

In contrast to the phantom reported in [17], the electrotextile-based design demonstrates enhanced flexibility, enhanced broadband performance, and improved mechanical robustness. As the electrotextile is directly embedded into the silicone-carbon substrate, the phantom is more resistant to bending and repeated deformations without the ground plane detachment or material breakdown. Note that the proposed solution is conceptually different from commercially available

bulky rigid phantoms (e.g. [31], [32]), primarily developed for static and dosimetric evaluations. While they excel in precisely replicating dielectric properties for a broad range of frequencies, they are often costly due to the significant amount of material required to manufacture anatomically correct models. In contrast, our phantom's flexibility and reconfigurability enable conformity to anatomical shapes and body positions with minimal material usage, significantly reducing both the cost and environmental footprint of the fabrication process.

Note that this phantom cannot be used for dosimetry and in-body power absorption evaluation. While this design is optimized for replicating the reflection from the skin surface, the presence of the conductive electrotextile alters the absorption characteristics, making the phantom unsuitable for dosimetric assessments. The applicability of the reflectivity-based phantoms tommW dosimetry was investigated in [27], [39], [40].

The proposed phantom opens new opportunities for body-centric measurements where flexible, conformal, reconfigurable or dynamic body models are needed. It is a promising solution for various applications, such as performance testing of wireless wearables or radars for remote human-centered sensing and monitoring.

REFERENCES

[1] N. Rendevski and D. Cassioli, "UWB and mmWave communication techniques and systems for healthcare," in *Ultra-Wideband and 60 GHz Communications for Biomedical Applications*, Y. Mehmet, Eds. New York, NY: Springer, 2014, pp. 1–22.

[2] "ETSI EN 302 567 V2.1.1," ETSI Standard EN 302 567 V2.1.1, European Telecommunications Standards Institute (ETSI), 07 2017.

[3] G. Conway, W. Scanlon, C. Orlenius, and C. Walker, "In situ measurement of UHF wearable antenna radiation efficiency using a reverberation chamber," *Antennas Wireless Propag. Lett.*, vol. 7, pp. 271–274, 2008.

[4] K. Fukunaga, S. Watanabe, H. Asou, and K. Sato, "Dielectric properties of non-toxic tissue-equivalent liquids for radiowave safety tests," in *Proc. IEEE Int. Conf. Dielectric Liquids*, Coimbra, Portugal, 2005, pp. 419–422.

[5] K. T. Z. Jian and H. Daigoro, "Development of ultra-wideband electromagnetic phantoms for antennas and propagation studies," in *Proc. 1st IEEE Eur. Conf. Antennas Propag.*, Dec. 2006, vol. 626, pp. 1–6.

[6] T. Yilmaz, T. Karacolak, and E. Topsakal, "Characterization and testing of a skin mimicking material for implantable antennas operating at ISM band (2.4 GHz-2.48 GHz)," *IEEE Antennas Wireless Propag. Lett.*, vol. 7, pp. 418–420, 2008.

[7] M. Y. Kanda, M. Ballen, S. Salins, C.-K. Chou, and Q. Balzano, "Formulation and characterization of tissue equivalent liquids used for RF densitometry and dosimetry measurements," *IEEE Trans. Microw. Theory Techn.*, vol. 52, no. 8, pp. 2046–2056, Aug. 2004.

[8] N. Chahat, M. Zhadobov, and R. Sauleau, "Broadband tissue-equivalent phantom for BAN applications at millimeter waves," *IEEE Trans. Microw. Theory Techn.*, vol. 60, no. 7, pp. 2259–2266, Jul. 2012.

[9] K. Guido, C. Matos, J. Ramsey, and A. Kiourti, "Tissue-emulating phantoms for in vitro experimentation at radio frequencies: Exploring characteristics, fabrication, and testing methods," *IEEE Antennas Propag. Mag.*, vol. 63, no. 6, pp. 29–39, Dec. 2021.

[10] N. N. Graedel, J. R. Polimeni, B. Guerin, B. Gagoski, and L. L. Wald, "An anatomically realistic temperature phantom for radiofrequency heating measurements: Realistic temperature phantom for radiofrequency heating measurements," *Magn. Reson. Med.*, vol. 73, pp. 442–450, Jan. 2015.

[11] J. Croteau, J. Sill, T. Williams, and E. Fear, "Phantoms for testing radar-based microwave breast imaging," in *Proc. IEEE 13th Int. Symp. Antenna Technol. Appl. Electromagn. Can. Radio Sci. Meeting*, Banff, AB, Canada, Feb. 2009, pp. 1–4.

[12] J. Chang, M. Fanning, P. Meaney, and K. Paulsen, "A conductive plastic for simulating biological tissue at microwave frequencies," *IEEE Trans. Electromagn. Compat.*, vol. 42, no. 1, pp. 76–81, Feb. 2000.

[13] G. Fixter, A. Treen, I. Youngs, and S. Holden, "Design of solid broadband human tissue simulant materials," *Int. Elect. Eng. Proc., Sci. Meas. Technol.*, Nov. 2022, vol. 149, no. 6, pp. 323–328.

[14] H. Tamura, Y. Ishikawa, T. Kobayashi, and T. Nojima, "A dry phantom material composed of ceramic and graphite powder," *IEEE Trans. Electromagn. Compat.*, vol. 39, no. 2, pp. 132–137, May 1997.

[15] Y. Nikawa, M. Chino, and K. Kikuchi, "Soft and dry phantom modeling material using silicone rubber with carbon fiber," *IEEE Trans. Microw. Theory Techn.*, vol. 44, no. 10, pp. 1949–1953, Oct. 1996.

[16] T. Hikage, Y. Sakaguchi, T. Nojima, and Y. Koyamashita, "Development of lightweight solid phantom composed of silicone rubber and carbon nanotubes," in *Proc. IEEE Int. Symp. Electromagn. Compat.*, Honolulu, HI, USA, Jul. 2007, pp. 1–4.

[17] A. R. Guraliuc, M. Zhadobov, O. De Sagazan, and R. Sauleau, "Solid phantom for body-centric propagation measurements at 60 GHz," *IEEE Trans. Microw. Theory Techn.*, vol. 62, no. 6, pp. 1373–1380, Jun. 2014.

[18] B. Mohammed et al., "Stable and lifelong head phantoms using polymer composition mimicking materials to test electromagnetic medical imaging systems," *IEEE J. Electromagn. RF Microw. Med. Biol.*, vol. 5, no. 4, pp. 322–328, Dec. 2021.

[19] D. Hintenlang and B. Terracino, "Tu-h-campus-iep2-05: Breast and soft tissue-equivalent 3D printed phantoms for imaging and dosimetry," *Med. Phys.*, vol. 43, no. 6, 2016, Art. no. 3781.

[20] T. Kairn, S. Crowe, and T. Markwell, "Use of 3D printed materials as tissue-equivalent phantoms," *Sci. Eng. Fac.*, vol. 51, pp. 728–731, 2015.

[21] P. Lamberti, L. Melillo, M. la Mura, R. Kotsilkova, V. Georgiev, and V. Tucci, "A 3D printed human skin phantom made of multifunctional nanocomposites for the assessment of RF treatments effect," in *Proc. IEEE Int. Workshop Metrol. Ind. 4.0 IoT*, 2021, pp. 335–340.

[22] S. Castelló-Palacios, C. Garcia-Pardo, A. Fornes-Leal, N. Cardona, and A. Vallés-Lluch, "Tailor-made tissue phantoms based on acetonitrile solutions for microwave applications up to 18 GHZ," *IEEE Trans. Microw. Theory Techn.*, vol. 64, no. 11, pp. 3987–3994, Nov. 2016.

[23] S. Romeo et al., "Dielectric characterization study of liquid based materials for mimicking breast tissues," *Microw. Opt. Technol. Lett.*, vol. 53, pp. 1276–1280, 2011.

[24] S. Castelló-Palacios, C. Garcia-Pardo, M. Alloza-Pascual, A. Fornes-Leal, N. Cardona, and A. Vallés-Lluch, "Gel phantoms for body microwave propagation in the (2 to 26.5) GHZ frequency band," *IEEE Trans. Antennas Propag.*, vol. 67, no. 10, pp. 6564–6573, Oct. 2019.

[25] A. Mirbeik-Sabzevari and N. Tavassolian, "Ultrawideband, stable normal and cancer skin tissue phantoms for millimeter-wave skin cancer imaging," *IEEE Trans. Biomed. Eng.*, vol. 66, no. 1, pp. 176–186, Jan. 2019.

[26] K. Sasaki et al., "Design of a skin equivalent phantom for estimating surface temperature elevation due to human exposure to electromagnetic fields from 10 to 100 GHZ," *IEEE Trans. Electromagn. Compat.*, vol. 63, no. 5, pp. 1631–1639, Oct. 2021.

[27] M. Ziane, A. Boriskin, C. Leconte, L. Le Coq, and M. Zhadobov, "Novel technique for in-body absorbed power density assessment based on free-space e-field measurement," *IEEE Trans. Microw. Theory Techn.*, vol. 72, no. 7, pp. 4127–4138, Jul. 2024.

[28] M. Zhadobov, N. Chahat, R. Sauleau, C. Le Quement, and Y. Le Drean, "Millimeter-wave interactions with the human body: State of knowledge and recent advances," *Int. J. Microw. Wireless Technol.*, vol. 3, pp. 237–247, Apr. 2011.

[29] K. Li, K. Sasaki, S. Watanabe, and H. Shirai, "Relationship between power density and surface temperature elevation for human skin exposure to electromagnetic waves with oblique incidence angle from 6 GHz to 1 THz," *Phys. Med. Biol.*, vol. 64, no. 6, 2019, Art. no. 065016.

[30] S. Gabriel, R. W. Lau, and C. Gabriel, "The dielectric properties of biological tissues: II. measurements in the frequency range 10 hz to 20 GHz," *Phys. Med. Biol.*, vol. 41, Nov. 1996, Art. no. 2251.

[31] SPEAG, "OTA phantoms - CTIA Above 3 GHz & mmWave," Accessed: Nov. 10, 2023. [Online]. Available: https://speag.swiss/products/em-phantoms/ctia-mmw/

[32] IT'IS Foundation, "Experimental Phantoms," Accessed: Nov. 6, 2023. [Online]. Available: https://itis.swiss/customized-research/experimental-phantoms/

[33] M. Zhadobov, C. Leduc, A. Guraliuc, N. Chahat, and R. Sauleau, "Antenna/human body interactions in the 60 GHz band: State of knowledge and recent advances," in *Advances in Body-Centric Wireless Communication: Applications and State-of-The-Art*, Q. H. Abbasi, M. Ur-Rehman, K. Qaraqe, and A. Alomainy, Eds. Stevenage, U.K.: IET, Jun. 2016, pp. 97–142.

[34] C. A. Balanis, *Advanced Engineering Electromagnetics*. Hoboken, NJ, USA: Wiley, 2012.

[35] G. Sacco, S. Pisa, and M. Zhadobov, "Age-dependence of electromagnetic power and heat deposition in near-surface tissues in emerging 5G bands," *Sci. Rep.*, vol. 11, no. 1, 2021, Art. no. 3983.

[36] G. Sacco, D. Nikolayev, R. Sauleau, and M. Zhadobov, "Antenna/human body coupling in 5G millimeter-wave bands: Do age and clothing matter?," *IEEE J. Microwaves*, vol. 1, no. 2, pp. 593–600, Apr. 2021.

[37] T. Dow Chemical Company, "Technical data sheet SYLGARD^{TM}184 silicone elastomer," 2017. [Online]. Available: https://www.dow.com/documents/11/11-3184-sylgard-184-elastomer.pdf?iframe=true

[38] M. Life Science S.A.S, "Safety data sheet sigma-aldrich 484164 carbon powder," 2023. [Online]. Available: https://www.sigmaaldrich.com/FR/en/sds/aldrich/484164?userType=anonymous

[39] M. Ziane, M. Zhadobov, and R. Sauleau, "High-resolution power density measurement technique in the near-field accounting for antenna/body coupling at millimeter-waves," *IEEE Antennas Wireless Propag. Lett.*, vol. 20, no. 11, pp. 2151–2155, Nov. 2021.

[40] M. Ziane, A. Boriskin, and M. Zhadobov, "Near-field power density mapping of close-to-body low-power mmwave devices," *IEEE Antennas Wireless Propag. Lett.*, vol. 22, no. 10, pp. 2347–2351, Oct. 2023.